AGU PUBLICATIONS

[Geophysical Research Letters]

Supporting Information for

Detection and attribution of human influence on the global diurnal temperature range decline

Jianyu Liu[1,2,3], Xingyu Feng[1], Xihui Gu[4,5,6], Jiawen Zhang[1], Louise J. Slater[6], Dongdong Kong[4,5]

[1]Laboratory of Critical Zone Evolution, School of Geography and Information Engineering, China University of Geosciences, Wuhan 430074, China

[2]State Key Laboratory of Water Resources and Hydropower Engineering Science, Wuhan 430074, China

[3]State Key Laboratory of Hydrology-Water Resources and Hydraulic Engineering, Nanjing Hydraulic Research Institute, China

[4]Department of Atmospheric Science, School of Environmental Studies, China University of Geosciences, Wuhan 430074, China

[5]Centre for severe weather and climate and hydro-geological hazards, Wuhan 430074, China

[6]School of Geography and the Environment, University of Oxford, South Parks Road, Oxford OX1 3QY, United Kingdom

Corresponding authors: Xihui Gu (guxh@cug.edu.cn); Dongdong Kong (kongdongdong@cug.edu.cn)

Contents of this file

Text S1 to S6

Text S1 HadEX3 data processing

We choose 1951–2018 as the period of analysis since observational data is relatively sparse before 1951 (Dunn et al., 2020). In addition, to improve the reliability of the computed DTR, we only consider the grid cells with adequate observations, covering over 70% of the years 1951–2018 (i.e., at least 48 years). The HadEX3 datset only includes stations ending after 2009 in the gridded product. As a result, there are relatively more missing data after 2009. Hence, following previous work, we added a restricted condition for the data during this period, i.e., at least five years during the period 2010–2018 (Dong et al., 2017). In a recent study (Tian et al., 2020), the global land surface was partitioned into ten regions. Given the lack of adequate long-term observations in the central areas of Africa (Figure 1), we consider two subcontinents of Africa instead, i.e., Northern Africa and South Africa. Hence, 11 regions are used in this study, i.e., East Asia, Europe, Middle East, North America, Northern Africa, Oceania, Russia, South America, South Asia, Southeast Asia, and Southern Africa. All selected continents and subcontinents have more than 75% of spatial data coverage. A total of 89.0% of the land surface grid cells (accounting for 86.5% of the land surface area) are employed to calculate the global mean, including valid observations during 1951–2018 (Figure S1).

Text S2 CMIP6 simulations and optimal fingerprinting technique

We use multimodel simulations from four experiments under the CMIP6 Detection and Attribution Model Intercomparison Project (DAMIP), including historical (i.e., ALL), hist-GHG (greenhouse gas forcing only), hist-AER (anthropogenic aerosol forcing), and hist-NAT (historical natural forcing only; including solar and volcanic), to detect and attribute the change in observations during 1951–2018. These experiments all cover the period of 1951–2018 except the ALL experiment. The ALL experiments from most models ended in 2014. To keep the consistency of coverage, we extend the ALL simulations by using simulations for 2015–2018 from the corresponding models from the Shared Socioeconomic Pathway (SSP) 2-4.5 scenario (Dong et al., 2021), which was used to force the hist-GHG and hist-AER simulations (Gillett et al., 2021). Furthermore, the anthropogenic forcing (ANT) simulations are obtained by subtracting NAT simulations from ALL simulations (Paik et al., 2020). To estimate changes in DTR in the future, we also use the projections (2018-2100) under SSP1-2.6, SSP3-7.0, and SSP5-8.5 scenarios. We select the same group of models for all the experiments (Table S1) except for the pre-industrial controls (CTL), which require a larger sample to estimate the range of scaling factor uncertainties (Paik et al., 2020). Hence, we used the CTL from all available models (a total of 25 models) to structure the noise covariance of internal variability. Overall, we used eight climate models that contain GHG, AER, and NAT experiments and SSP scenarios, and 200 non-overlapping chunks of 68-year length from CTL in the analysis. All these simulations are interpolated to the same 1.875°×1.25° grid. To ensure a fair comparison with observations, we used only the grid cells with valid observations to space-time mask all model simulations.

We applied a two-way detection of ANT and NAT by regressing observed trends onto the ANT and NAT simultaneously. In addition, to separate the impacts of specific anthropogenic forcings, we conducted four-way detection by regressing observed trends onto GHG, AER, NAT, and OANT (other ANT, e.g., ozone and land use change; OANT = ALL-GHG-AER-NAT) simultaneously. The two-way and four-way detections are used to test whether multiple forcings are jointly detectable and whether the detected signal can be separated from other forcings, as well as internal variability (Paik et al., 2020). The attributable trends in each signal are calculated using the trends in the annual time series multiplied by the scaling factors (Gillett et al., 2021; Hegerl and Zwiers, 2011).

To control for spatiotemporal heterogeneity, we reduce the dimensions of observations and simulations at both spatial and temporal scales (Dong et al., 2021). Spatially, the anomalies for the grid cells with valid observations are computed as the area-weighted average over the globe and within the 11 regions. Temporally, following previous work (Gillett et al., 2021; Paik et al., 2020), non-overlapping 5-year means were used to reduce the time dimension, which results in 14 temporal points during

1951–2018 for each region and the globe. Using 5-year means is a compromise between shortening the temporal dimension and reducing the variability in the observation and noise in the signals (Zhang et al., 2019), and retaining important natural forcings (Yin et al., 2017) such as volcanoes (Wan et al., 2019). Limited by the time series length, the last temporal point only uses a 3-year (i.e., 2016–2018) mean. For South America there are few observations in the first decade, so only 12 temporal points are used, covering the period 1961–2018.

Text S3 DTR data from different sources and their changes

Due to the scarcity of stations, there are no valid observations in HadEX3 dataset over some regions, such as Africa and the Middle East. Hence, we also use three other meteorological datasets, i.e., Princeton Global Forcing, Berkeley Earth Surface Temperature, and CRU TS, to investigate the robustness of the detection and attribution results. These three datasets were produced based on different observations, and the interpolations have been applied at both temporal and spatial scales (Thorne et al., 2016). Hence, these three datasets have valid values for all land-surface grids.

The Berkeley Earth Surface Temperature dataset is based on observations from 12 sources, including Tmax and Tmin. The dataset provides monthly Tmax and Tmin covering 1880-2021 at 1°×1° spatial resolution (Rohde et al., 2013). The gridded data is obtained by applying a Kriging interpolation. This dataset can be downloaded from http://berkeleyearth.org/data/.

The CRU TS dataset provides ten meteorological variables, including the DTR variable, which is calculated as Tmax – Tmin (Harris et al., 2020). As CRU TS strives for completeness over the land, sparse areas are filled using the available values in 1961-1990 climatology. The station-scale data are interpolated to 1°×1° spatial resolution by Delaunay Triangulation (Harris et al., 2020). We used the latest version 4.04, which covers the period of 1901-2019. This dataset is available from https://data.ceda.ac.uk/badc/cru/data/cru_ts/cru_ts_4.04.

The Princeton Global Forcings dataset is made by merging a series of observation-based and reanalysis datasets (Sheffield et al., 2006). The biases are corrected using observation-based datasets. The dataset provides 3-hourly, daily, and monthly meteorological variables, including Tmax and Tmin, which are downscaled in space with consideration of elevation. The data covers the period of 1948-2016, and can be downloaded from http://hydrology.princeton.edu/data/pgf/v3/.

Generally, the four datasets support the finding that DTR decreased in most regions (Figure S1). The spatial patterns of changes in DTR from HadEX3, CRU TS, and Princeton Global Forcings are roughly consistent, and the percentages of grids showing significant decreasing trends are in agreement, with 50.7%, 52.6%, and 52.7%, respectively. However, the DTR trends from the Berkeley Earth Surface Temperature dataset have relatively large differences compared to the other datasets. This may be because the Berkeley Earth Surface Temperature dataset uses many stations with short-term observations that are not included in other datasets (Thorne et al., 2016), as well as different station selection and interpolation methods. The regions with distinct differences between datasets are mainly located in Greenland, South America, and South Asia, where available observations are limited in these regions.

Text S4 Quantile delta mapping (QDM) bias correction algorithm

Given that simulations from global climate models (GCMs) have considerable systematic biases compared with observations, we applied a bias correction algorithm, i.e., quantile delta mapping (QDM), to correct these biases. QDM is an integrated approach that combines quantile delta change (Olsson et al., 2009), quantile perturbation (Willems and Vrac, 2011), and detrended quantile mapping methods (Bürger et al., 2012). The detrended annual time series are used to build the quantile mapping between simulations and observations. Then the trends in the simulations are recovered by multiplying the bias-corrected simulations with the trends in the uncorrected simulations, to effectively reduce systematic biases and simultaneously preserve the relative change in simulations (Cannon, 2015). This approach mainly includes three steps as follows.

Firstly, the time series are detrended and then rearranged by scaling and rescaling.

$$\hat{x}_{m,p}(t) = F_{o,h}^{-1}\left\{F_{m,h}\left[\frac{\bar{x}_{m,h}x_{m,p}(t)}{\bar{x}_{m,p}(t)}\right]\right\}\frac{\bar{x}_{m,p}(t)}{\bar{x}_{m,h}} \quad (1)$$

where $\bar{x}_{m,h}$ is the mean value of simulation during the historical period and the $\bar{x}_{m,p}(t)$ is the projected period at the time of t. The $F_{o,h}$, and $F_{m,h}$ are the cumulative distribution functions (CDFs) of observed data $x_{o,h}$ and modeled data $x_{m,h}$ in the historical period, respectively.

Second, the bias in the non-exceedance probability quantile ($\tau_{m,p}$) at time t is corrected by using the inverse CDF of observations during the historical period ($x_{o,h}$).

$$\hat{x}_{o:m,h:p}(t) = F_{o,h}^{-1}\left[\tau_{m,p}(t)\right] \quad (2)$$

Last, the projection quantiles changes are transferred to the bias-corrected simulations, by using the relative change $\Delta_m(t)$ multiplied by its historical bias-corrected value (Cannon et al., 2015).

$$\hat{x}_{m,p}(t) = \hat{x}_{o:m,h:p}(t) \times \frac{x_{m,p}(t)}{F_{m,h}^{-1}\left[\tau_{m,p}(t)\right]} \quad (3)$$

As shown by Hawkins and Sutton (2009), the dominant source of uncertainty in the GCM outputs comes from the model structure, which is larger than that of the scenario and ensemble. As a result, the outputs from a specific model can share similar biases, even under different forcing experiments (Yuan et al., 2018). Therefore, QDM is first applied to correct the CDFs of ALL (historical) experiment to the observed CDFs; and then the same CDFs of ALL simulations are applied to correct the simulations under different forcings and the projections under different scenarios (Yuan et al., 2018). The bias correction is conducted for each model independently.

Before applying the bias correction, the climate model simulations were processed to the same spatial resolution as the observations (1.875°×1.25°). Then to verify the reliability of the bias corrections, we assessed the performance of corrected simulations in reproducing the observations in terms of both interannual variability and trends during 1951-2018. In addition, we also applied the imperfect model test to verify the performance of the bias-corrected projections during 2019-2100. We regarded the simulations of each model in turn as pseudo-observations, and applied them to correct the bias in the simulations from other models. The bias correction algorithm is calibrated for each grid cell during the historical period (1951-2018) and then used to correct the projections during 2019-2100. The Root Mean Square Error (RMSE) was used to assess the performance of the corrected simulations.

Text S5 Changes in simulated DTR from CMIP6

The NAT simulations show mixed increases and decreases in DTR with a weak trend, implying limited impacts of NAT on changes in DTR (Figure 1c). Consequently, the spatial patterns of ANT trends are almost the same as those of ALL trends (Figure 1d). In contrast, AER simulations possess increasing trends over most considered areas (67.9%). AER significantly increases the DTR over Europe and North America, where aerosol emissions were reduced in recent decades (Subba et al., 2020). The increase in DTR induced by the decline in aerosol emissions can partly counteract the negative effects of GHG. As a result, the DTR trends in ANT and ALL simulations are slightly weaker than those in GHG simulations over Europe and North America. Generally, the ALL simulations underestimate the observed changes in DTR. However, the variations in observations are mostly within the 95% confidence intervals of ALL simulations (Figure S3).

The observed trend in the global DTR (-0.43°C/68 y) is far from the simulated trends from individual CTL simulations (Figures S7a), suggesting that the observations may exceed the range expected from internal variability. The observed trend falls outside of the trend simulated under NAT forcing (0℃/68 years) (Figure S7b; Figure S3a). The magnitude of the decrease in observations is larger than the median trend of ALL ensembles, but still in the range of simulated trends from individual models (Figure S7b-d). Besides, over 72.4% of global grids, the ALL simulations from most (more than 5) models show consistent trends with the observed ones (Figure S8).

Text S6 The impacts of ENSO on detection results

The El Niño Southern Oscillation (ENSO) is the leading mode of natural climate variability and is an important factor regulating regional and global climate. Hence, ENSO may also influence changes in the DTR, as well as the detection and attribution results. Here, linear regression is used to regress the observed annual DTR to ENSO (Wang and Toumi, 2021), represented using the Oceanic Nino Index (ONI, https://origin.cpc.ncep.noaa.gov/products/analysis_monitoring/ensostuff/ONI_v5.php):

$$DTR_{sim} = \beta_0 ENSO + \beta_1 \quad (1)$$

where β_0 and β_1 are the regression coefficients; and DTR_{sim} is the simulated DTR. Then the ENSO-residual observations, i.e., observed DTR minus DTR_{sim}, were used to analyze the effect of removing ENSO (Gudmundsson et al., 2017).

Figure S15 shows the time series of DTR with and without removing the impacts of ENSO. Generally, there are little differences in the trends between observations and ENSO-residual observations over the globe and most subcontinents, suggesting ENSO has negligible impacts on DTR trends. Furthermore, we also examine the sensitivity of detection and attribution results using the ENSO-residual observations (Figure S16–S17). The results based on the ENSO-residual observations are very similar to those based on the original observations, with a minor improvement in the scaling factor for some regions (e.g., East Asia and Russia), where the scaling factors are closer to unity (Figure S18). These results suggest that ENSO has a limited impact on DTR trends, as well as the detection and attribution result. Similar results were also found in Min et al. (2011).

Figures S1 to S15

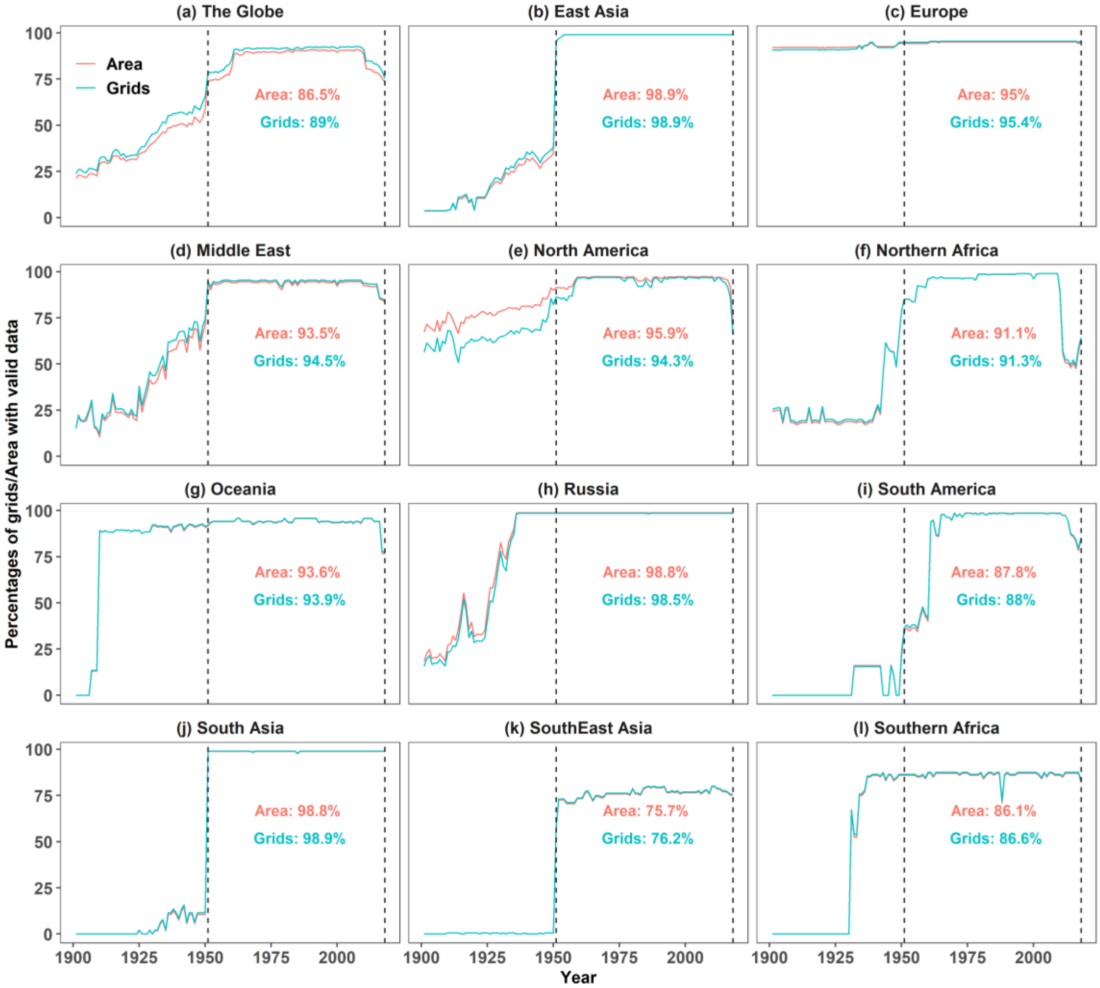

Figure S1. Percentages of land surface area and grid cells including valid observations. The percentages are calculated as the numbers (area) of grids with valid data divided by the total number (area) of grids for each year over the globe and each subcontinent. The two dotted vertical lines represent the years 1951 and 2018.

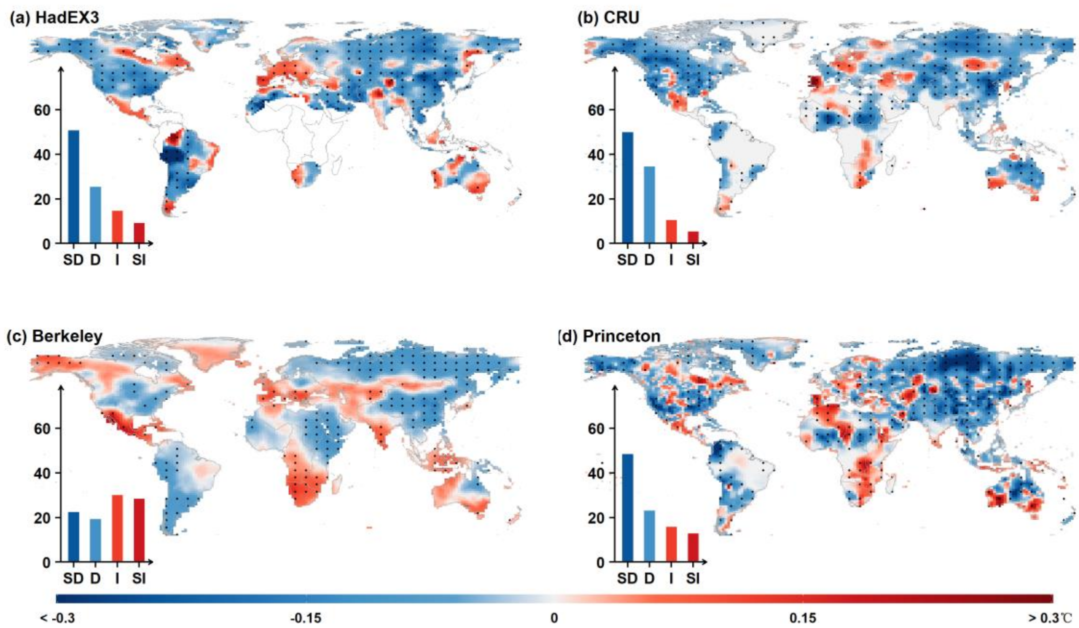

Figure S2. Spatial distribution of trends (℃/decade) in observed DTR from different datasets, i.e., HadEX3, CRU, Berkeley, and Princeton. Limited by temporal coverage, the DTR from Princeton only covers the periods of 1951-2016, while the other three datasets all cover the periods of 1951-2018. The inset histogram summarizes the area proportions showing a significant decrease (SD), decrease (D), increase (I), and significant increase (SI) in DTR, respectively.

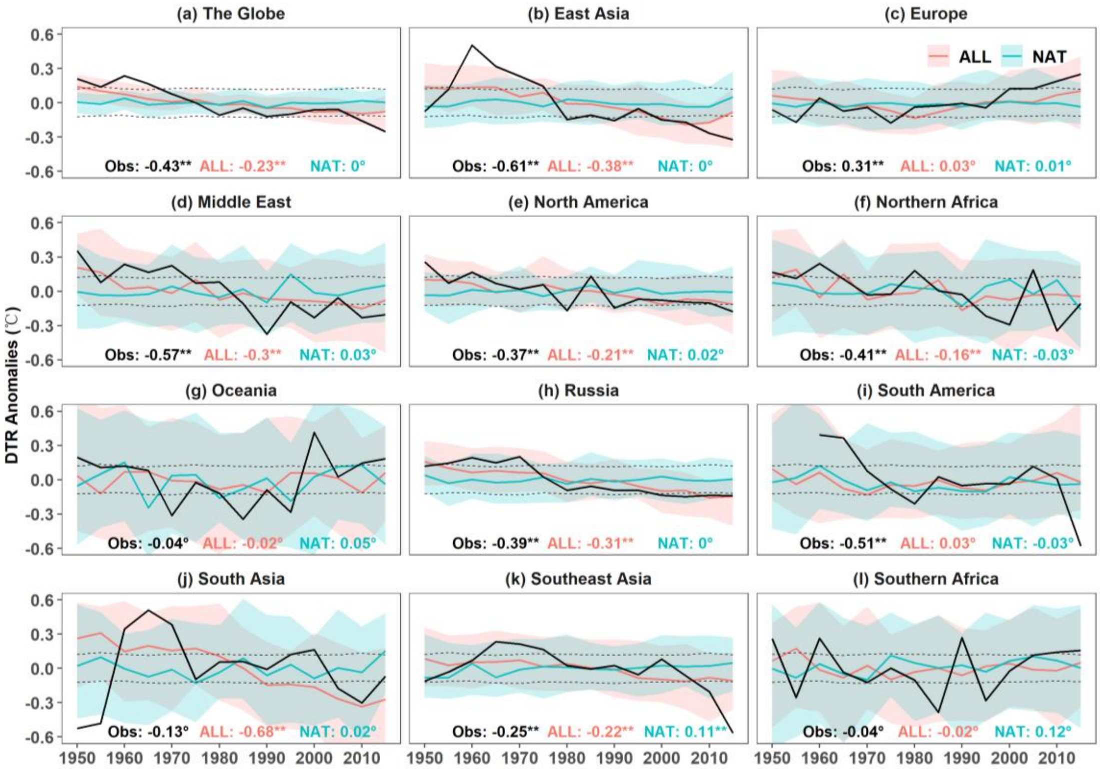

Figure S3. Timeseries of DTR from observation and simulations. The time series indicate five-year-mean anomalies from observations and simulations with ALL (red) and NAT (blue) forcing, as well as their 95% confidence intervals (shadings). The black line represents the observed DTR. The horizontal gray dotted lines represent the 5-95% quantiles of internal variability from the pre-industrial unforced (CTL) control simulations. The long-term trends (℃ per 68 years) for observations, ALL, and NAT are shown at the bottom of each panel. The symbols "*" and "**" indicate the trends are significant at the 95% and 99% confidence level, respectively; while "°" indicates the trends are not significant at the 95% confidence level.

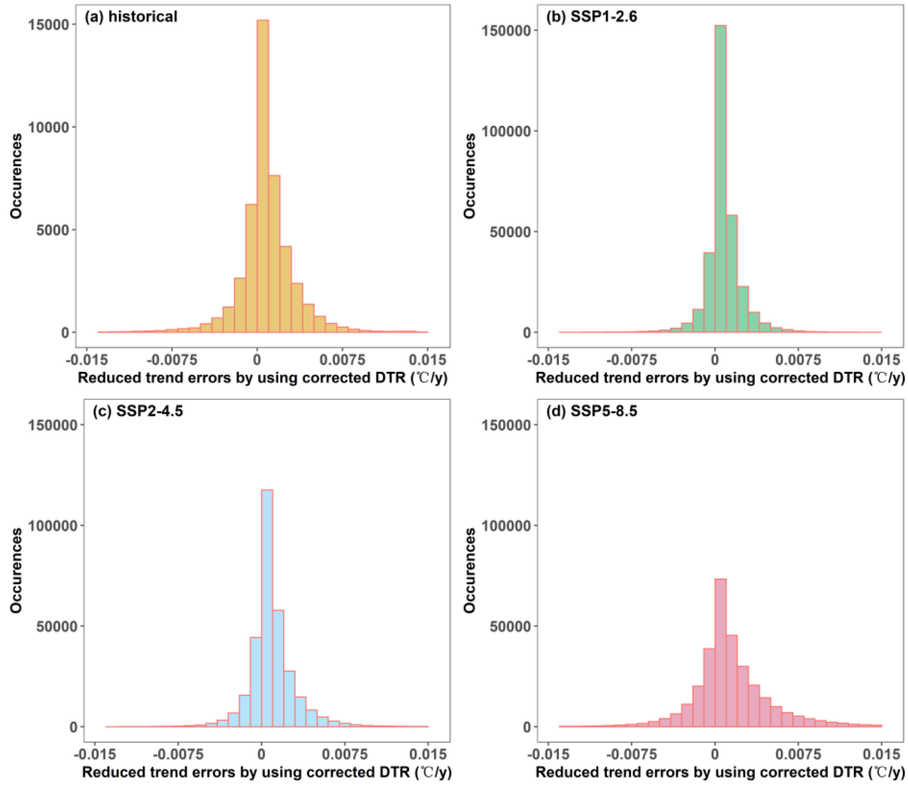

Figure S4. The reduction in trend errors after applying QDM bias correction. The trend errors are calculated by comparing the trend in corrected and uncorrected simulations to the trend in (a) observations during 1951-2018 and (b-d) pseudo-observations during 2019-2100 for each grid. In panel (a), we corrected the bias of historical simulations from 8 climate models based on the observed annual DTR. In panels (b-d), we perform the bias correction by using an imperfect model test, withholding one model at a time and regarding its outputs as pseudo-observations, and applying it to correct the simulations from the other seven models; the bias correction is obtained for each grid during the historical period (1951-2018) and then used to correct the projections during 2019-2100.

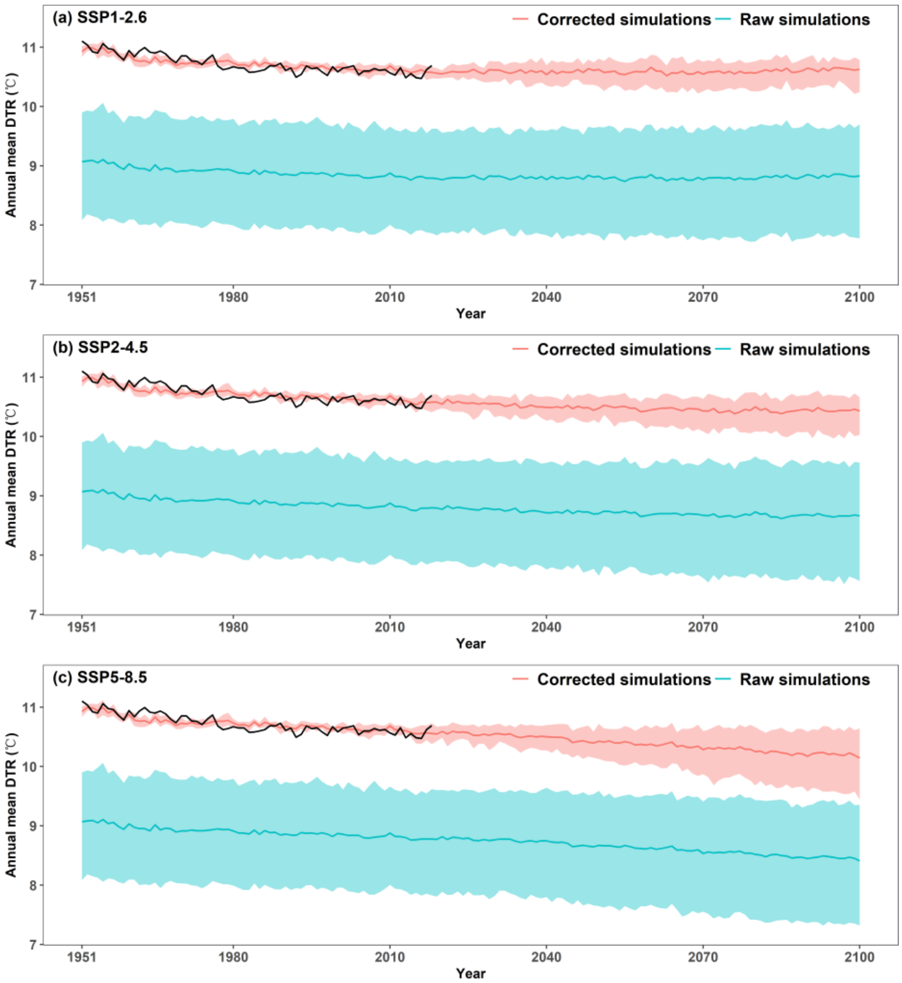

Figure S5. Comparison between the raw and corrected simulations and the observations. The color time series are the multimodel simulations under ALL forcing during 1951-2014 combined with the multimodel simulations during 2015-2100 under (a) SSP1-2.6, (b) SSP2-4.5, and (c) SSP5-8.5. The red (blue) lines and their shadings are the multimodel mean of QDM-based corrected (uncorrected) simulations and their corresponding 5-95% ranges. The black lines are the time series of HadEX3 observations.

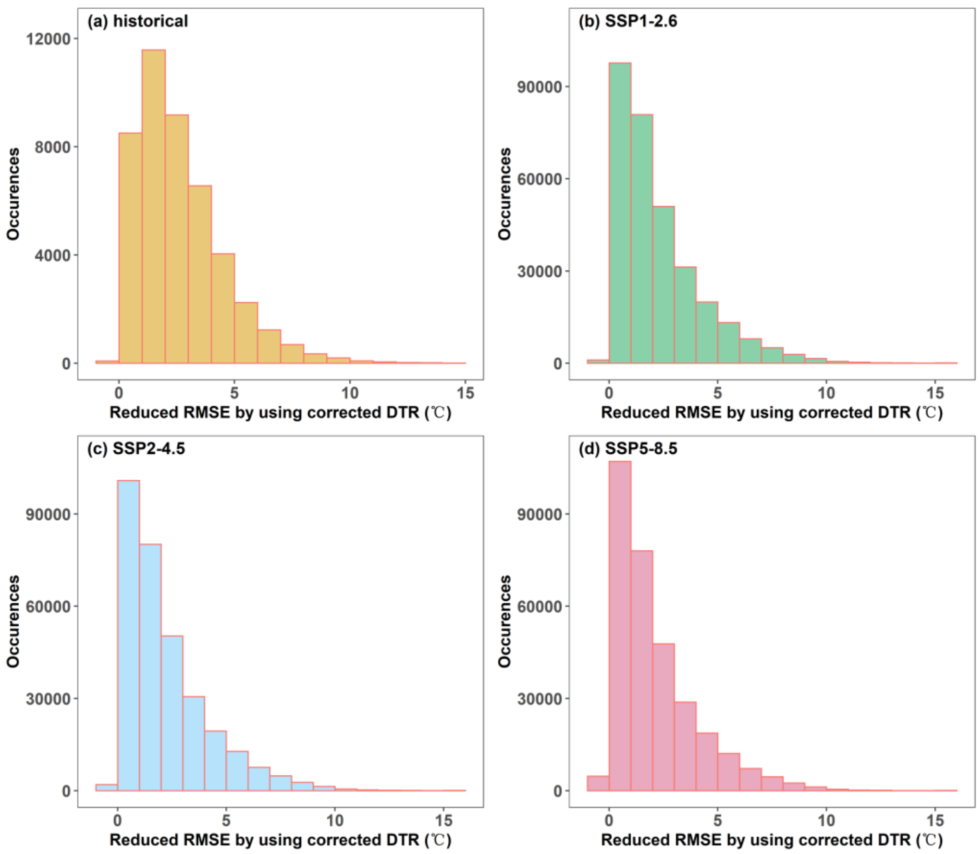

Figure S6. Reduced RMSE after bias correction. The RMSE is calculated between the simulations and (a) observations during 1951-2018 and (b-d) pseudo-observations during 2019-2100 for each grid cell. In panel (a), we correct the bias of simulations from 8 climate models based on the observed annual DTR. In panels (b-d), we perform the bias correction by using an imperfect model test, withholding one model at a time and regarding its outputs as pseudo-observations, and applying it to correct the simulations from the other seven models.

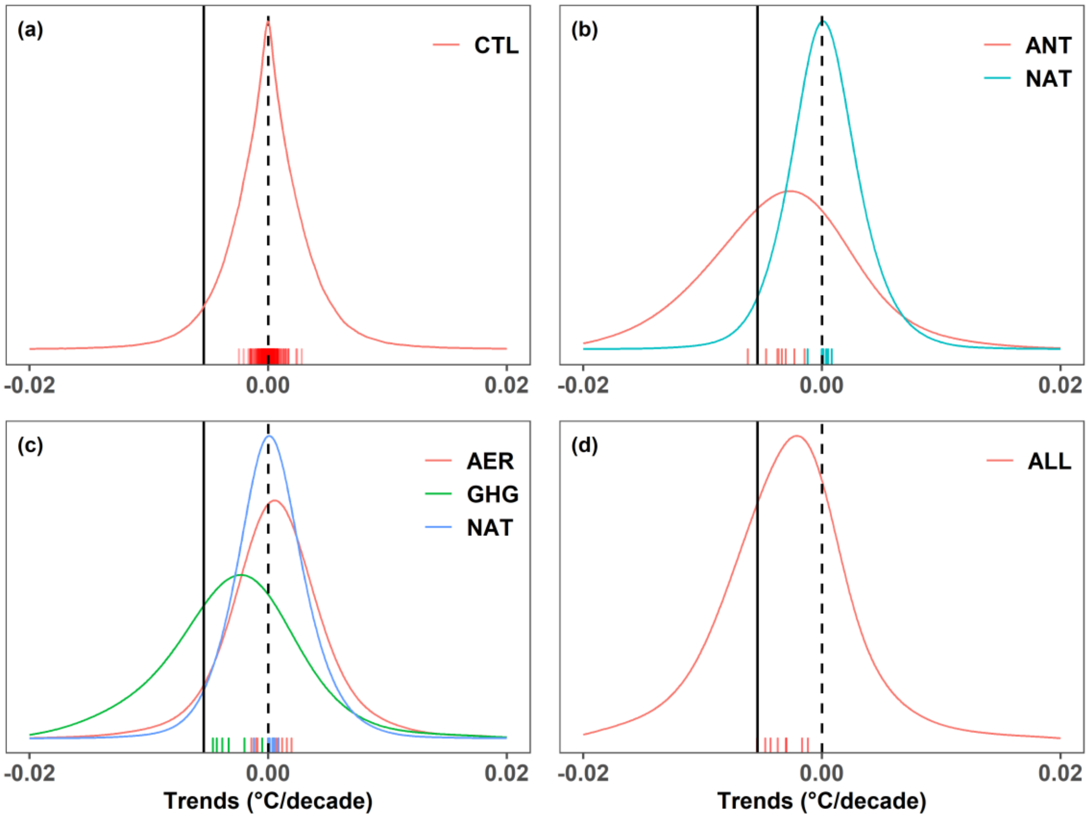

Figure S7. Probability density of trends in simulations under different forcings across the globe. The curves are the Gaussian-fitted probability density of trends for all grids over the global considered land surface area. The vertical black line represents the observed DTR trend. The black dashed line represents zero. The short vertical color lines represent the trend estimates from individual climate models.

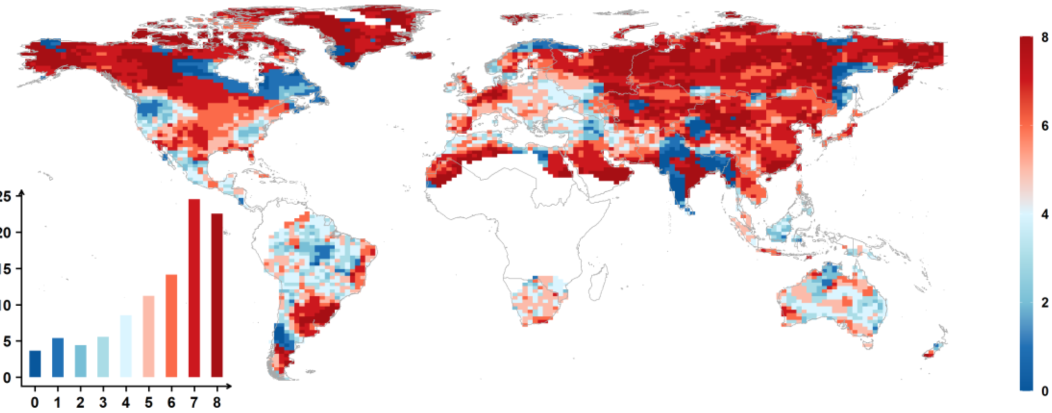

Figure S8. The number of models with simulations showing a consistent trend sign with the observed trend during 1951-2018. The inset histogram shows the proportion of grids in which 0–8 models show a consistent trend with the observed trend.

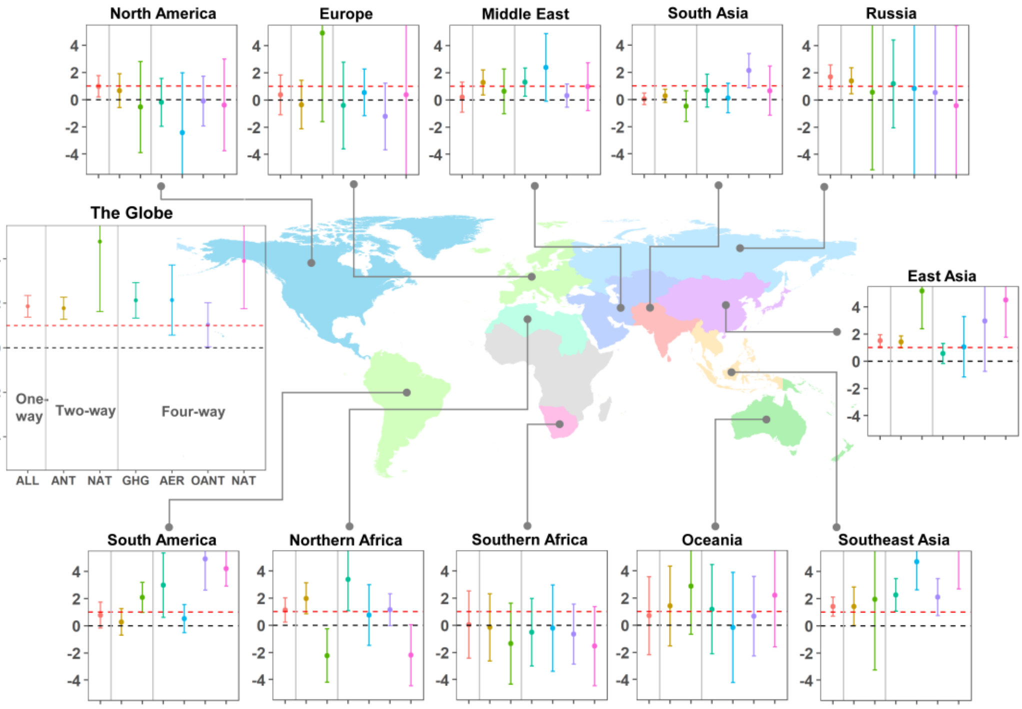

285
286 **Figure S9.** The same as Figure 2, but during 1951-2014.
287

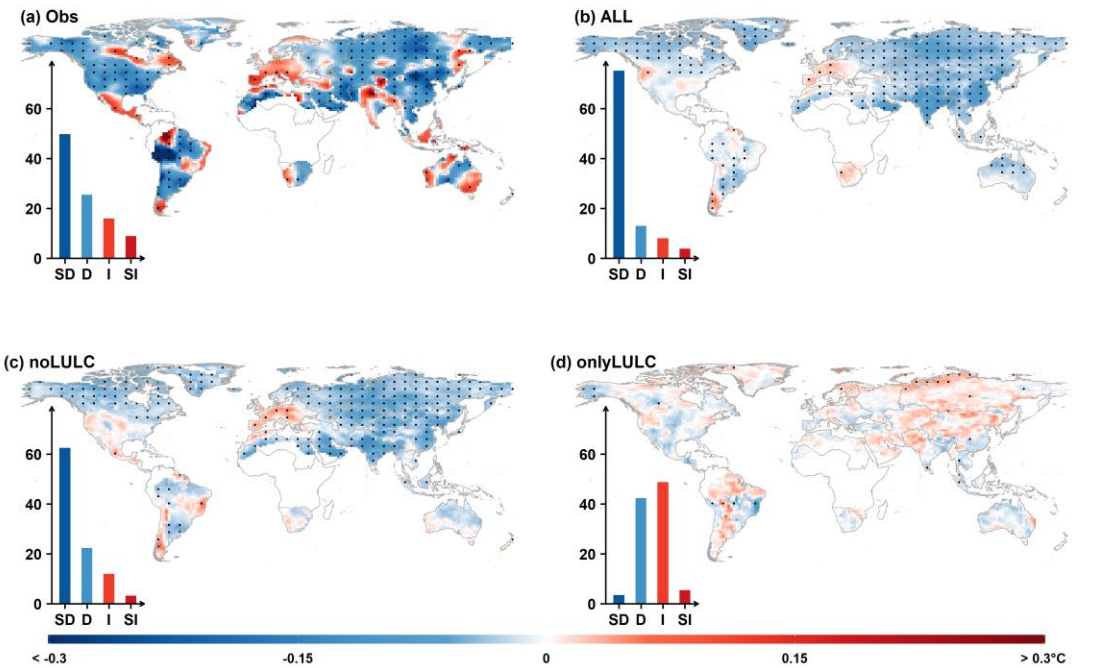

Figure S10. Spatial distribution of trends (℃/decade) in DTR during 1951-2014. Trends in (a) observed DTR (Obs); and trends in CMIP6 multimodel ensemble mean simulations with: (b) historical all forcing (ALL), (c) historical with no land use and land cover change (noLULC), (d) historical with only land use and land cover change (onlyLULC). The inset histograms summarize the percentage of the land surface showing a significant decrease (SD), decrease (D), increase (I), and significant increase (SI) in DTR, respectively. Noting that the simulations (ending in 2014) in this figure are from Land-Use Model Intercomparison Project (LUMIP) in CMIP6.

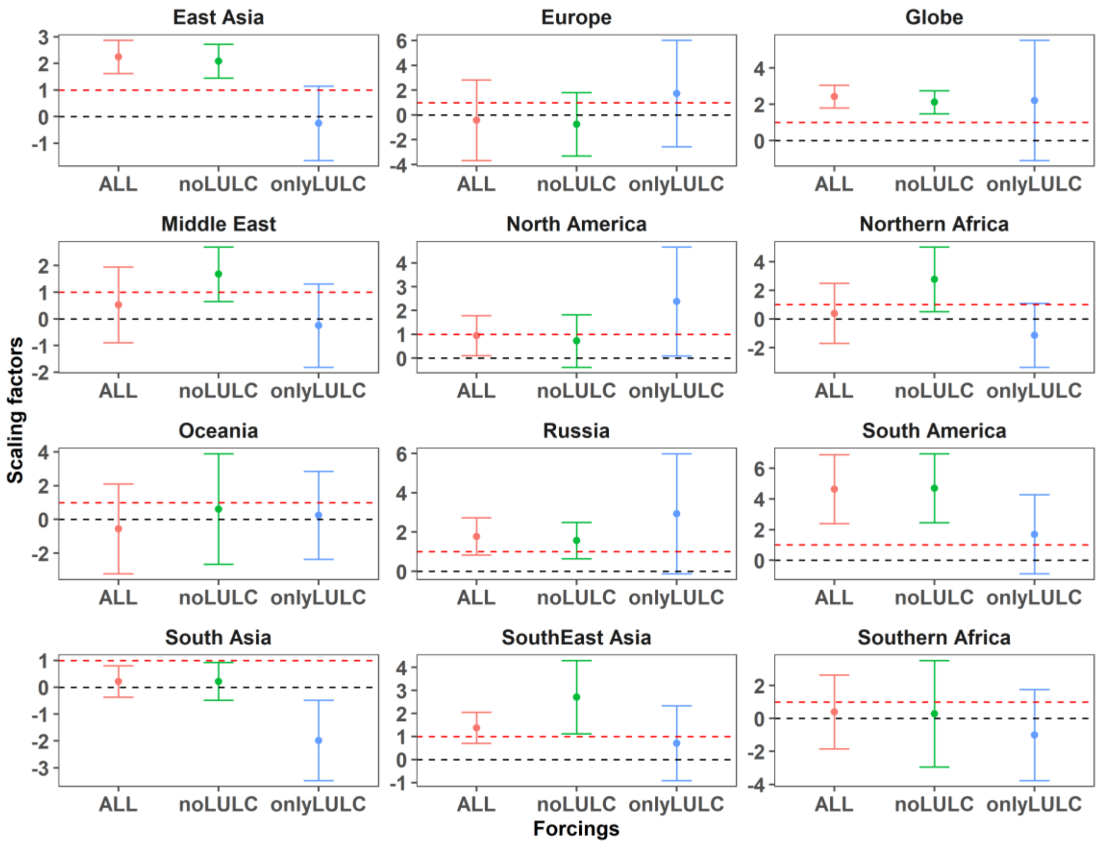

Figure S11. Optimized scaling factors and their 95% confidence intervals during 1951-2014. The observations are regressed onto ALL simulations by one-way detection, onto historical with no land use and land cover change (noLULC) and historical with only land use and land cover change (onlyLULC) by two-way detection. The horizontal black and red dashed lines indicate zero and unity, respectively. When the 95% confidence interval of the scaling factor lies above zero this indicates the corresponding signal can be detected in the observed DTR, and a scaling factor larger than one suggests that the simulated trend underestimates the observed one. Noting that the simulations (ending in 2014) in this figure are from Land-Use Model Intercomparison Project (LUMIP) in CMIP6.

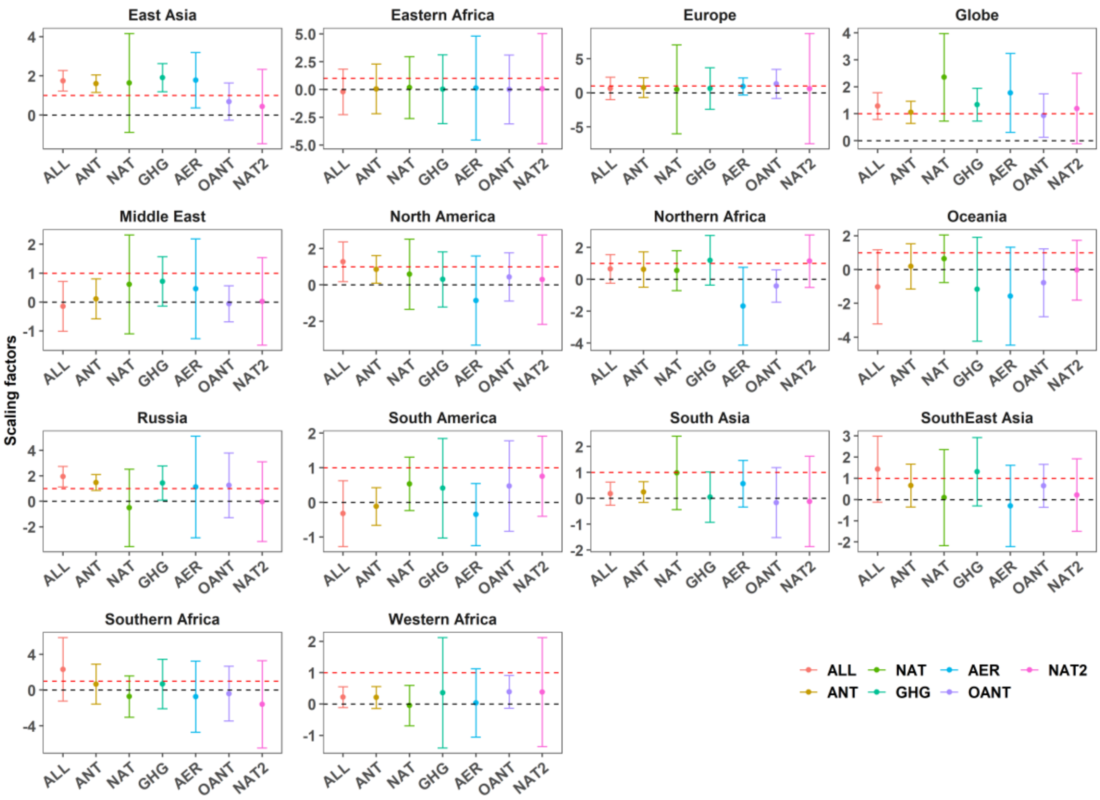

Figure S12. Optimized scaling factors and their 95% confidence intervals during 1951-2018. Observed DTR is from the mean of three datasets, that is CRU, Berkeley, and Princeton. The observations are regressed onto ALL simulations by one-way detection, onto ANT and NAT by two-way detection, and onto GHG, AER, OANT, and NAT by four-way detection. The horizontal black and red dashed lines indicate zero and unity, respectively. When the 95% confidence interval of the scaling factor lies above zero this indicates the corresponding signal can be detected in the observed DTR, and a scaling factor larger than one suggests that the simulated trend underestimates the observed one.

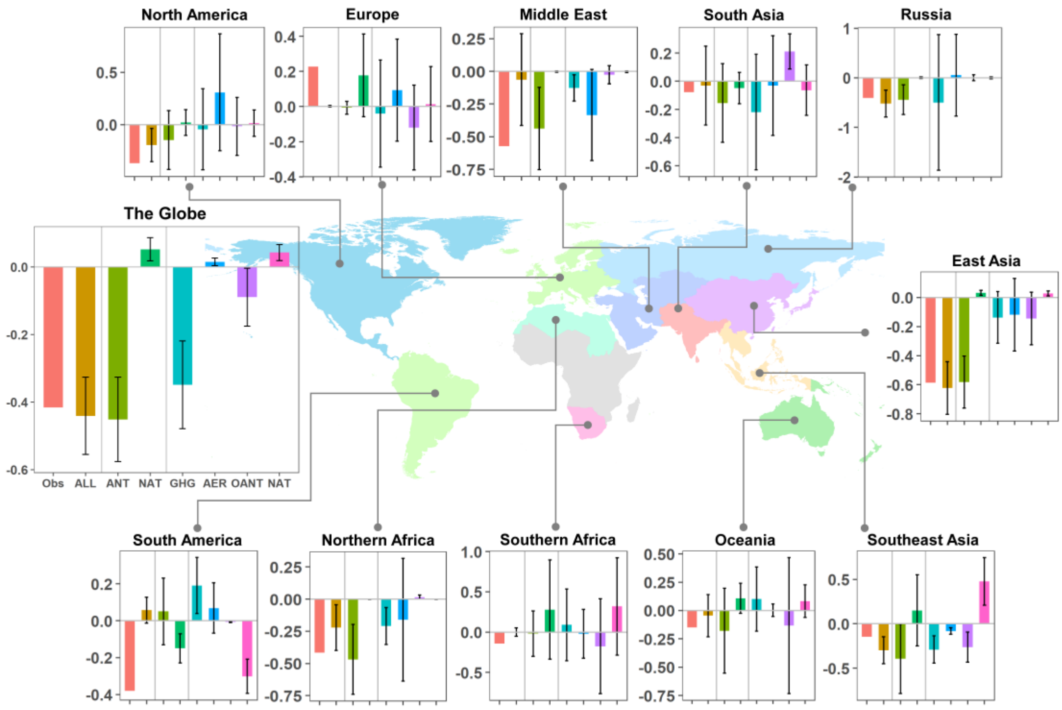

Figure S13. The same as Figure 3, but during 1951-2014.

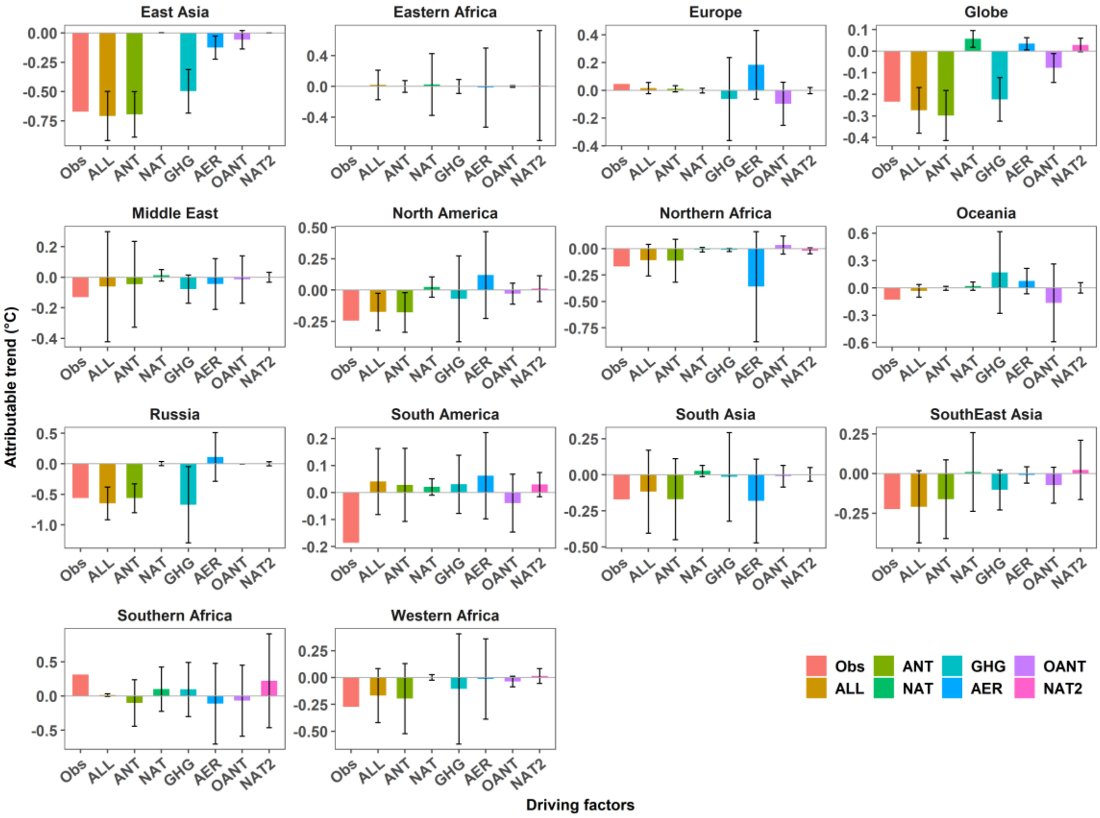

Figure S14. Observed annual DTR trends and their drivers during 1951-2018. Observed DTR is from the mean of three datasets, that is CRU, Berkeley, and Princeton. Attributable change is calculated by multiplying the annual trends by the corresponding scaling factors. Error bars are the corresponding 95% confidence intervals.

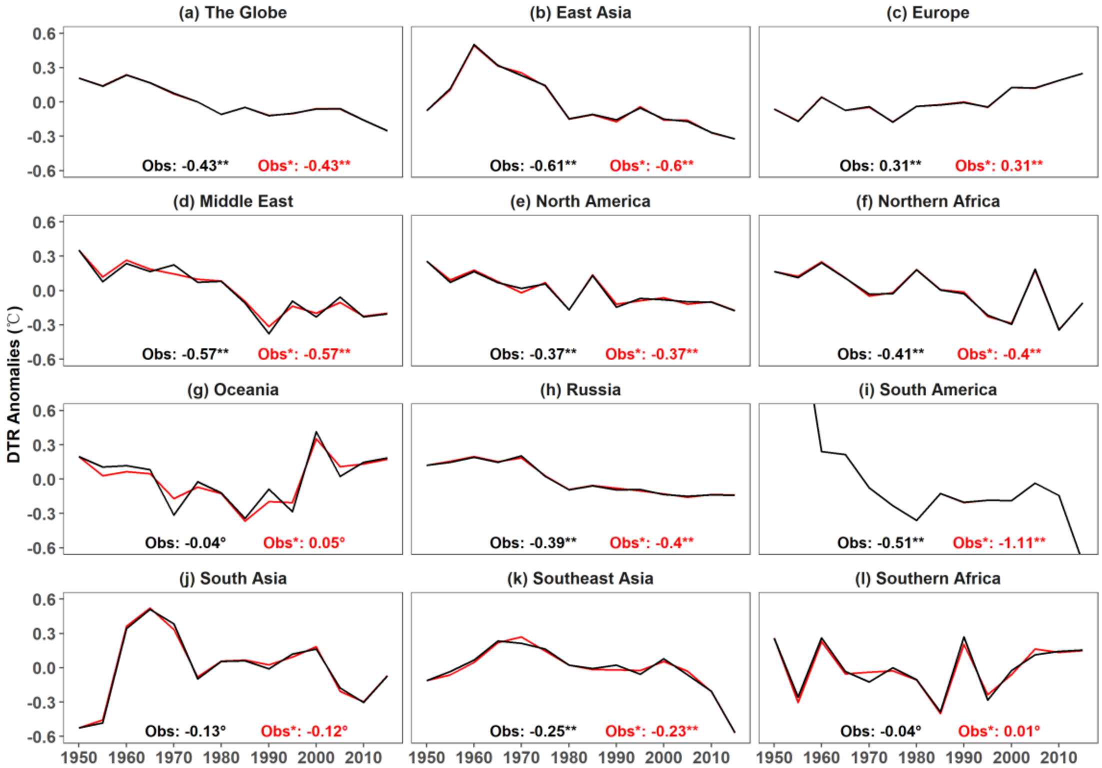

Figure S15. Time series of DTR from observations (Obs) and ENSO-residual observations (Obs*). The black and red lines represent the five-year-mean anomalies of observations and ENSO-residual observations, respectively. The long-term trends (°C per 68 years) for observations and ENSO-residual observations are shown at the bottom of each panel. The symbols "*" and "**" indicate trends that are significant at the 95% and 99% confidence level, respectively; while "°" indicates trends that are not significant at the 95% confidence level.

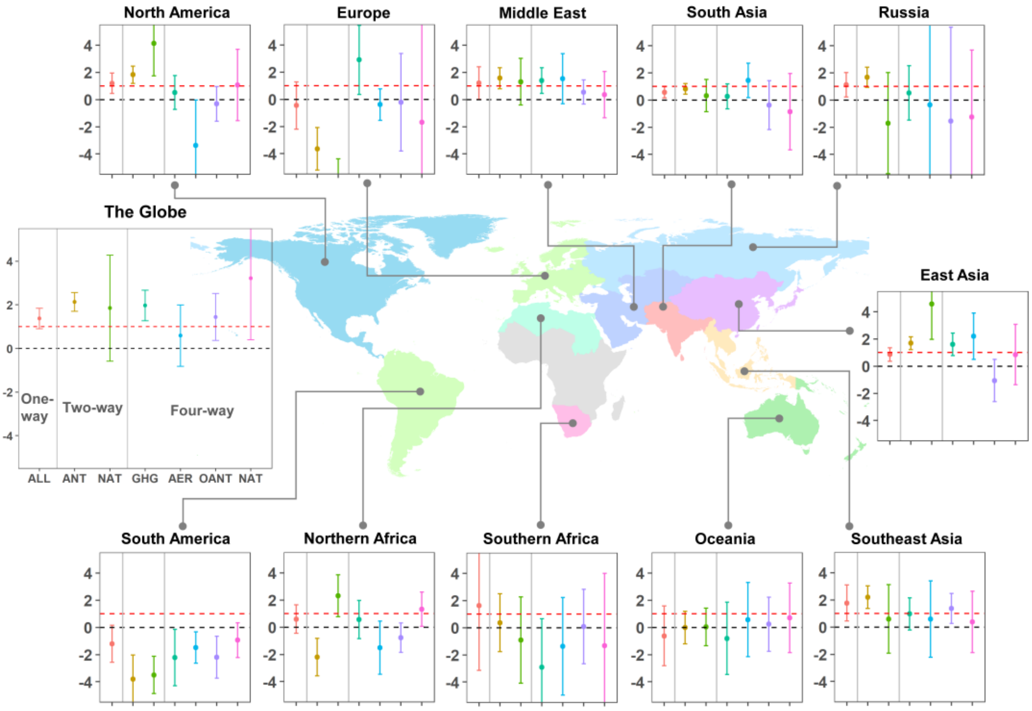

Figure S16 The same as Figure 2, but for the ENSO-residual observations, instead of the observations.

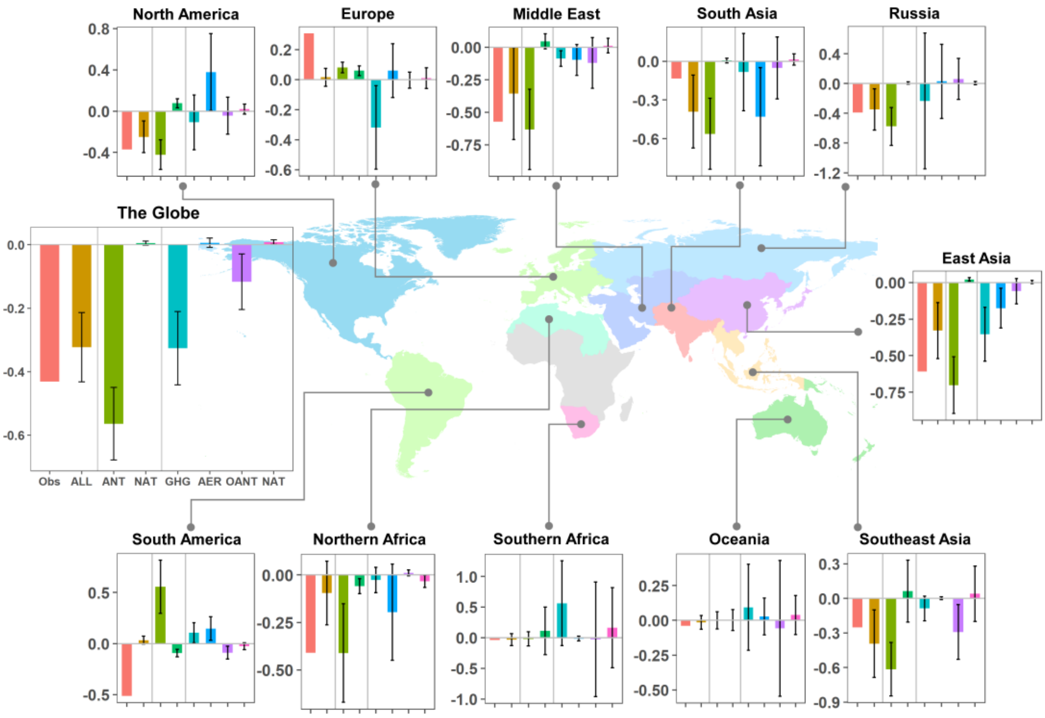

Figure S17 The same as Figure 3, but for the ENSO-residual observations, instead of the observations.

Table S1

Table S1. List of global climate model simulations used in this study.

Model	AER	GHG	NAT	ANT	ALL	SSP 1-2.6	SSP 3-7.0	SSP 5-8.5
ACCESS-ESM1-5	◆	◆	◆	◆	◆	◆	◆	◆
BCC-CSM2-MR	◆	◆	◆	◆	◆	◆	◆	◆
CanESM5	◆	◆	◆	◆	◆	◆	◆	◆
FGOALS-g3	◆	◆	◆	◆	◆	◆	◆	◆
GFDL-ESM4	◆	◆	◆	◆	◆	◆	◆	◆
IPSL-CM6A-LR	◆	◆	◆	◆	◆	◆	◆	◆
MIROC6	◆	◆	◆	◆	◆	◆	◆	◆
MRI-ESM2-0	◆	◆	◆	◆	◆	◆	◆	◆

References

Bürger, G., Murdock, T. Q., Werner, A. T., Sobie, S. R., & Cannon, A. J. (2012). Downscaling Extremes—An Intercomparison of Multiple Statistical Methods for Present Climate. *Journal of Climate*. *25*(12), 4366-4388. https://doi.org/10.1175/jcli-d-11-00408.1

Cannon, A. J. (2015). An intercomparison of regional and at-site rainfall extreme value analyses in southern British Columbia, Canada. *Canadian Journal of Civil Engineering*. *42*(2), 107-119. https://doi.org/10.1139/cjce-2014-0361

Cannon, A. J., Sobie, S. R., & Murdock, T. Q. (2015). Bias correction of GCM precipitation by quantile mapping: how well do methods preserve changes in quantiles and extremes? *Journal of Climate*. *28*, 6938-6959. https://doi.org/ https://doi.org/10.1175/JCLI-D-14-00754.1.

Dong, B., Sutton, R. T., & Shaffrey, L. (2017). Understanding the rapid summer warming and changes in temperature extremes since the mid-1990s over Western Europe. *Climate Dynamics*. *48*(5-6), 1537-1554. https://doi.org/10.1007/s00382-016-3158-8

Dong, S. Y., Sun, Y., Li, C., Zhang, X. B., Min, S. K., et al. (2021). Attribution of Extreme Precipitation with Updated Observations and CMIP6 Simulations. *Journal of Climate*. *34*(3), 871-881. https://doi.org/10.1175/jcli-d-19-1017.1

Dunn, R. J. H., Alexander, L. V., Donat, M. G., Zhang, X., Bador, M., et al. (2020). Development of an Updated Global Land In Situ-Based Data Set of Temperature and Precipitation Extremes: HadEX3. *Journal of Geophysical Research-Atmospheres*. *125*(16). https://doi.org/10.1029/2019jd032263

Gillett, N. P., Kirchmeier-Young, M., Ribes, A., Shiogama, H., Hegerl, G. C., et al. (2021). Constraining human contributions to observed warming since the pre-industrial period. *Nature Climate Change*. *11*(3), 207–212. https://doi.org/10.1038/s41558-020-00965-9

Harris, I., Osborn, T. J., Jones, P., & Lister, D. (2020). Version 4 of the CRU TS monthly high-resolution gridded multivariate climate dataset. *Scientific Data*. *7*(1). https://doi.org/10.1038/s41597-020-0453-3

Hegerl, G., & Zwiers, F. (2011). Use of models in detection and attribution of climate change. *Wiley Interdisciplinary Reviews-Climate Change*. *2*(4), 570-591. https://doi.org/10.1002/wcc.121

Min, S.-K., Zhang, X., Zwiers, F. W., & Hegerl, G. C. (2011). Human contribution to more-intense precipitation extremes. *Nature*. *470*(7334), 378-381. https://doi.org/10.1038/nature09763

Olsson, J., Berggren, K., Olofsson, M., & Viklander, M. (2009). Applying climate model precipitation scenarios for urban hydrological assessment: A case study in Kalmar City, Sweden. *Atmospheric Research*. *92*(3), 364-375. https://doi.org/https://doi.org/10.1016/j.atmosres.2009.01.015

Paik, S., Min, S. K., Zhang, X. B., Donat, M. G., King, A. D., et al. (2020). Determining the Anthropogenic Greenhouse Gas Contribution to the Observed Intensification of Extreme Precipitation. *Geophysical Research Letters*. *47*(12), 12. https://doi.org/10.1029/2019gl086875

Rohde, R., R., M., R., J., S., P., A., R., et al. (2013). Berkeley Earth temperature averaging process. *Geoinform. Geostat*, doi:10.4172/gigs.1000103, 1. https://doi.org/doi:10.4172/gigs.1000103

Sheffield, J., Goteti, G., & Wood, E. F. (2006). Development of a 50-year high-resolution global dataset of meteorological forcings for land surface modeling. *Journal of Climate*. *19*(13), 3088-3111. https://doi.org/10.1175/jcli3790.1

Subba, T., Gogoi, M. M., Pathak, B., Bhuyan, P. K., & Babu, S. S. (2020). Recent trend in the global distribution of aerosol direct radiative forcing from satellite measurements. *Atmospheric Science Letters*. *21*(11). https://doi.org/10.1002/asl.975

Thorne, P. W., Donat, M. G., Dunn, R. J. H., Williams, C. N., Alexander, L. V., et al. (2016). Reassessing changes in diurnal temperature range: Intercomparison and evaluation of existing global data set estimates. *Journal of Geophysical Research-Atmospheres*. *121*(10), 5138-5158. https://doi.org/10.1002/2015jd024584

Tian, H. Q., Xu, R. T., Canadell, J. G., Thompson, R. L., Winiwarter, W., et al. (2020). A comprehensive quantification of global nitrous oxide sources and sinks. *Nature*. *586*(7828), 248-256. https://doi.org/10.1038/s41586-020-2780-0

Wan, H., Zhang, X. B., & Zwiers, F. (2019). Human influence on Canadian temperatures. *Climate Dynamics*. *52*(1-2), 479-494. https://doi.org/10.1007/s00382-018-4145-z

Wang, S., & Toumi, R. (2021). Recent migration of tropical cyclones toward coasts. *Science*. *371*(6528), 514-417. https://doi.org/10.1126/science.abb9038

Willems, P., & Vrac, M. (2011). Statistical precipitation downscaling for small-scale hydrological impact investigations of climate change. *Journal of Hydrology*. *402*(3), 193-205. https://doi.org/https://doi.org/10.1016/j.jhydrol.2011.02.030

Yin, H., Sun, Y., Wan, H., Zhang, X. B., & Lu, C. H. (2017). Detection of anthropogenic influence on the intensity of extreme temperatures in China. *International Journal of Climatology*. *37*(3), 1229-1237. https://doi.org/10.1002/joc.4771

Yuan, X., Jiao, Y., Yang, D. W., & Lei, H. M. (2018). Reconciling the Attribution of Changes in Streamflow Extremes From a Hydroclimate Perspective. *Water Resources Research*. *54*(6), 3886-3895. https://doi.org/10.1029/2018wr022714

Zhang, J. P., Zhao, T. B., Dai, A. G., & Zhang, W. Y. (2019). Detection and Attribution of Atmospheric Precipitable Water Changes since the 1970s over China. *Scientific Reports*. *9*. https://doi.org/10.1038/s41598-019-54185-z